

GRB Afterglows In The Multi-Messenger Era OR Electromagnetic Afterglows Of Structured Jets OR Structured Jets At All Angles

GEOFFREY RYAN¹ AND HENDRIK VAN EERTEN

¹*Joint Space-Science Institute, University of Maryland, College Park, MD 20742, USA*

ABSTRACT

Gamma-ray bursts (GRBs) associated with gravitational wave events are, and will likely continue to be, viewed at a larger inclination than their fellow GRBs without gravitational wave detections. As demonstrated by the afterglow of GW170817A, this requires an extension of the common GRB afterglow models which typically assume emission from an on-axis top hat jet. We present a characterization of the afterglows arising from structured jets, utilizing both trans-relativistic numerical calculations and simple analytic approximations. In many cases the temporal slope before the jet break is found to be a simple function of the ratio between the viewing angle and effective half opening angle of the jet. This provides a useful handle in the analysis of structured GRB afterglow light curves, but does not completely resolve the degeneracy between viewing angle and jet structure model. Our models, both numerical and analytic, are publicly available as the open source Python package `afterglowpy`.

1. INTRODUCTION

Gamma-ray burst (GRB) afterglows are commonly modeled as top hat blast waves with no internal structure pointed directly at the observer. This has been largely sufficient given the available data, although some evidence of viewing angle effects has been found (Ryan et al. 2015). ~~New observational capabilities have witnessed new phases of afterglow evolution, such as the discovery of plateaus with Swift.~~ Real jets (of course) have internal structure, but the top hat assumption has been a sufficiently spherical cow.

GW170817A changes the picture: new object with a strange afterglow. Steep/late rise, LONG slow rise, turnover at 160d. The slow rise is impossible to reproduce with standard afterglow evolution: first observation of a *structured* phase of evolution.

The dominant contribution may be an angular distribution of energy within the blast wave (“structured jet”) combined with off-axis viewing (CITE Rossi04). For GW170817A this corresponds to the “successful jet” picture. Alternately, radial stratification of velocity (“refreshed shock”) can cause a similar phase, most simply with a quasi-spherical (or at least top-hat) angular structure. This situation is produced by the “choked jet” or “cocoon” picture of GW170817A. Understanding the effects of both structures on afterglows, and their

dependence on the parameters of the burst, are vital to understanding GW counterparts.

To this end, we have calculated the power law temporal slope of the structured phase in both angular and radial structure dominated cases, along with the corresponding observed break times. We have developed a semi-analytic numerical model of structured GRB afterglows for detailed comparison to data, which is now publicly available.

Summary: In section 2 we discuss structured jets, in section 3 refreshed shocks, in section 4 our numerical model, section 5 application to GW170817A, and section 6 future applications and discussion.

2. MOTIVATION: WHY STRUCTURED JETS?

The *structured jet* is a GRB emission model where the isotropic-equivalent energy of a blast wave is a function of the angle from the jet axis: $E_{\text{iso}} = E(\theta)$. The specific structure of a jet is determined by the intrinsic structure of the jet launching mechanism as well as the sculpting that occurs as the jet burrows out of the encasing ejecta debris (as in a binary neutron star merger) or stellar envelope (as in a collapsar).

Numerical simulations have revealed a variety of jet angular energy distributions, often containing an energetic core with power law tails. Figure 1 shows a collection of jet energy distributions from the literature (Aloy et al. 2005; Mizuta & Aloy 2009; Duffell & MacFadyen 2013; Lazzati et al. 2017; Margutti et al. 2018). Lacking a well-established physical model of the true $E(\theta)$, in particular its dependence on the parameters of the

Corresponding author: Geoffrey Ryan
gsryan@umd.edu

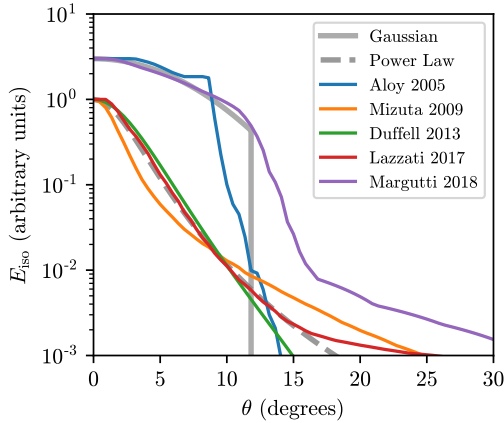


Figure 1. Lateral profiles of isotropic equivalent energy E_{iso} as a function of angle from the jet axis θ , individually rescaled to group similar profile shapes. The thick grey lines show fiducial profiles with simple analytic expressions (Equations (1) and (2)) while the thin colored lines show results from numerical simulations and analytic models chosen from the literature. The blue line is the B1 numerical simulation of Aloy et al. (2005), orange the HE16N numerical simulation of Mizuta & Aloy (2009), green an analytic “boosted fireball” model with $\gamma_B = 10$ and $\eta_0 = 3$ from Duffell & MacFadyen (2013), red the numerical simulation from Lazzati et al. (2017) (L17), and purple the numerical simulation from Margutti et al. (2018) (M18). The thick solid grey line is a Gaussian profile (Equation (1)) with $E_0 = 3 \times 10^{52}$ erg, $\theta_c = 6^\circ$, and $\theta_w = 12^\circ$ and the thick dashed grey line is a smoothed power law profile (Equation (2)) with $E_0 = 10^{52}$ erg, $\theta_c = 4^\circ$, $\theta_w = 20^\circ$, and $b = 4.5$. The Gaussian and power law profiles can emulate the basic properties of the energy profiles found in the literature.

system, we consider two simple parameterized models: a Gaussian jet and a power law with a smooth core.

$$E(\theta) = E_0 \exp\left(-\frac{\theta^2}{2\theta_c^2}\right) \quad \text{Gaussian} \quad (1)$$

$$E(\theta) = E_0 \left(1 + \frac{\theta^2}{\theta_c^2}\right)^{-b/2} \quad \text{power law} \quad (2)$$

Each fiducial model is parameterized by a normalization E_0 , a width θ_c , and a truncation angle θ_w . The power law model also retains a power law index b . Outside θ_w the energy is initially zero, this acts as an outer truncation angle for the jet.

Figure 1 shows an example of each model together with jet energy profiles drawn from the literature, mostly the result of numerical relativistic hydrodynamic simulations. The Gaussian profile emulates jets with a flat core and sharp edges, typically the result of powerful successful jets (Aloy et al. 2005; Margutti et al. 2018). Jets which are subject to stronger interactions

with the surrounding medium can develop a profile with energetic wings and a narrow core, emulated by the analytic power law profile (Mizuta & Aloy 2009; Duffell & MacFadyen 2013; Lazzati et al. 2017).

A generic energy profile $E(\theta)$ may have several more parameters, but one can still associate an on-axis energy $E_0 = E(0)$ and an effective core width $\theta_c \sim |E''(0)/E_0|^{-1/2}$ which should fully specify the leading order near on-axis behaviour.

The afterglow light curve of a structured jet follows one of two qualitatively different regimes depending on the orientation of the viewer with respect to θ_c . We refer to the regimes as “aligned” when $\theta_{\text{obs}} < \theta_c$, and “misaligned” when $\theta_{\text{obs}} > \theta_c$.

3. METHODS AND THE `afterglowpy` PACKAGE

To compute the light curves of structured jet afterglows we constructed numerical and analytic models utilizing the single shell approximation of van Eerten et al. (2010); van Eerten (2018). This approach integrates over the massive ejecta, contact discontinuity, and forward shock complex, treating it as a single fluid element with uniform radial structure. We utilize a trans-relativistic equation of state which smoothly interpolates between the ultra-relativistic and non-relativistic limits and include an approximate prescription for jet spreading. This approach, with a simplified equation of state and jet spreading model, has been used successfully to model the synthetic light curves of top hat jets from multidimensional numerical relativistic hydrodynamics simulations (van Eerten et al. 2010).

In the ultra-relativistic limit the single shell approximation provides useful scaling relations to compute the structured jet closure relations presented in Section 4. The full trans-relativistic numerical model is publicly available as the `afterglowpy` Python package, described in more detail in Section 3.2.

We utilize a standard spherical coordinate system (r, θ, ϕ) with origin at the GRB central engine and polar axis aligned with the jet axis. The blast wave forward shock has a radial position $R(t, \theta)$, where t is the time measured in the burster frame. The observer is located in a direction $\hat{\mathbf{n}}$ which makes an angle θ_{obs} with the z -axis, $\hat{\mathbf{n}} \cdot \hat{\mathbf{z}} = \cos \theta_{\text{obs}}$, and is oriented along the x -axis, $\phi_{\text{obs}} = 0$. A particular point on the blast wave $\hat{\mathbf{r}} = (\theta, \phi)$ makes an angle ψ (with cosine μ) with the viewer, $\mu = \cos \psi = \hat{\mathbf{n}} \cdot \hat{\mathbf{r}}$.

3.1. The Single Shell Approximation

The observed flux $F_\nu(t_{\text{obs}}, \nu_{\text{obs}})$ at observer time t_{obs} and frequency ν_{obs} is calculated via:

$$F_\nu(t_{\text{obs}}, \nu_{\text{obs}}) = \frac{1+z}{4\pi d_L^2} \int d\Omega dr r^2 \delta^2 \epsilon'_{\nu'} , \quad (3)$$

where z is the redshift of the source, d_L is the luminosity distance, δ the doppler factor of the emitting fluid with respect to the observer, and $\epsilon'_{\nu'}$ the fluid rest-frame emissivity.

To accommodate an initial structure profile $E(\theta)$ we consider the integrand of Equation (3) as a function of the polar angle θ . We assume each constant θ annulus evolves independently, as an equivalent top hat of width $\theta_c = \theta$. This is a very good approximation when transverse velocities are low: when the blast wave is ultra-relativistic and has not begun to spread and when the blast wave is non-relativistic and the spreading has ceased (van Eerten et al. 2010). Once jet spreading begins in earnest the errors are larger, and this approach can be best viewed as an interpolation between the correct ultra-relativistic and non-relativistic limits (van Eerten et al. 2010).

To compute the light curve of a top-hat jet of width θ we first must calculate the time evolution of the blast wave. In the single-shell approximation we treat the ejecta mass, contact discontinuity, and forward shock as a single unit propagating through a cold ambient medium with constant rest-mass density $\rho_0 = m_p n_0$. The forward shock is a radius R from the explosion and moves at a velocity β_s . In terms of the fluid four-velocity behind the shock u and its Lorentz factor γ this may be written as:

$$\dot{R} = \frac{4u\gamma}{4u^2 + 3} c. \quad (4)$$

Here the time derivative \dot{R} is taken with respect to elapsed time in the bursters' frame t .

The evolution of the four velocity is determined through conservation of energy. The total energy in the trans-relativistic single shell approximation is:

$$E = (\gamma - 1)M_{\text{ej}}c^2 + \frac{4\pi}{9}\rho_0c^2R^3(4u^2 + 3)\beta^2\Omega. \quad (5)$$

In Equation (5) the first term is the kinetic energy of the ejected mass M_{ej} , assumed to have already accelerated and adiabatically cooled to its coasting velocity. The second term is the kinetic and thermal energy of the shocked ISM with three-velocity $\beta = u/\gamma$. The shocked ISM is confined to a cone of solid angle $\Omega = 2\sin^2(\theta_0/2)$ where θ_0 is the half-opening angle of the jet. While the blast wave is relativistic θ_0 is constant, but once the jet edge comes in causal contact with the core it begins to spread due to its own internal pressure until the blast wave is spherical. The spreading occurs at sound speed c_s in the fluid rest-frame (van Eerten et al. 2010; Duffell & Laskar 2018):

$$\dot{\theta}_0 = \frac{c_s}{\gamma R}, \quad \text{if } u < 1/3\theta_c \text{ and } \theta_0 > \pi/2. \quad (6)$$

The criterion $u < 1/3\theta_0$ is satisfied when enough time has elapsed that a sound wave can propagate from $\theta = \theta_c$ to $\theta = 0$ in a blast wave propagating in a uniform ISM (CITE HENDRIK). It is similar to the condition given in Duffell & Laskar (2018), which found a numerical factor of 2.5 (instead of 3) after calibrating to numerical simulations. Our criteria differs from that used in (CITE Troja+) which used an overly simplistic $u < 1$ criterion to begin jet spreading.

Given a (possibly constant) expression for E Equation (5) may be differentiated with respect to t and solved for \dot{u} . In a refreshed shock scenario $E = E_>(u)$, whereas for a standard energy injection model one may take $E \propto t^{-q}$. In either case, Equation (5) produces an equation for \dot{u} . This defines a three dimensional system of ordinary differential equations in the variables (R, u, θ_0) which may be solved numerically or, in certain limits, analytically.

Once the shock evolution is known, the flux is given by the integral:

$$F_{\nu}(t_{\text{obs}}, \nu_{\text{obs}}) = \frac{1+z}{4\pi d_L^2} \int d\Omega R^2 \Delta R \delta^2 \epsilon'_{\nu'}, \quad (7)$$

where ΔR (TODO: add eq for Delta R) is the shock width contributing to the emission. The integrand is evaluated at a constant observer time t_{obs} and observer frequency ν_{obs} , related to t and ν' by:

$$t_{\text{obs}} = (1+z)(t - \mu(\theta, \phi)R(t)/c), \quad (8)$$

$$\nu_{\text{obs}} = (1+z)^{-1}\delta\nu', \quad (9)$$

TODO: Give formulae or reference for $\epsilon'_{\nu'}$.

The integral (7) may now be computed numerically or, in certain limits, analytically.

3.2. afterglowpy

The integral (7) is evaluated numerically using an adaptive Romberg integrator in each dimension, with a typical relative tolerances of 10^{-6} .

We have constructed the `afterglowpy` Python package to implement the numerical computation of light curves according to Section 3.1 and provide it to the community. The integration routine itself is written in C, wrapped as an extension for Python, and has been optimized to be used in intensive data analysis routines such as Markov Chain Monte-carlo which can require many thousands of evaluations.

`afterglowpy` uses a standard RK4 algorithm to evolve the $(R(t), u(t), \theta_0(t))$ system of equations on a fixed logarithmically spaced grid of t . The endpoints of the t -grid are chosen to bracket the burster frame times required to calculate the requested t_{obs} with at least a decade of

tolerance. Initial conditions for R , u , and θ_0 are those of a decelerating ultra-relativistic blast wave. The user can set the density of the t -grid with the n_t parameter: the number of grid points per decade of t . The default value for n_t is 1000, which is sufficiently dense that the **shock ODE evolution** is not the dominant error source but not so dense as to adversely impact performance.

Each top-hat jet component is integrated in θ and ϕ using an adaptive Romberg scheme with a fixed relative tolerance and an adaptive absolute tolerance. When summing over top-hat components of a structured jet, the innermost (core) component is calculated first. As the calculation proceeds, the current running sum of the flux is used to set absolute tolerance in the Romberg integrator for each component. **This minimizes the computations performed on dim, off-axis sectors of the jet.**

Each evaluation of the integrand requires a binary search to determine the burster time t at which to evaluate R , u , and θ_0 . Fluid quantities are then calculated using the shock-jump conditions and the synchrotron emissivity is evaluated using the standard external shock formulae (Granot & Sari 2002; van Eerten et al. 2010).

The numerical accuracy of a top-hat light curve with this scheme is typically better than 10^{-4} . The structured jet calculation splits the integration domain into N_θ disjoint annuli, each evaluated as an independent top-hat and summed. By default N_θ is chosen such that there will be 5 zones per θ_c -sized interval. The choice of N_θ has the largest impact on the code performance and accuracy. We find the choice $N_\theta = 5$ gives sufficiently quick performance at acceptable errors, typically on the order of 10^{-2} . TODO SHOW CONVERGENCE PLOT

3.3. Comparison To BoxFit

`afterglowpy`, in utilizing the semi-analytic methods of Section 3.1, trades some amount of physical accuracy for great flexibility. We gauge this trade-off by comparing to the `BoxFit` code, a standard tool which calculates high fidelity afterglow light curves based on numerical simulations.

Figure 2 shows a comparison between top-hat light curves calculated with `afterglowpy` and `BoxFit`. The `BoxFit` code uses two-dimensional relativistic hydrodynamic simulations to fully capture the non-linear hydrodynamics of a decelerating blast wave and a ray tracing radiative transfer module to compute observed synchrotron light curves. Figure 2 shows the light curve of a $\theta_c = 0.1\text{rad}$ top-hat at radio and x-ray frequencies (10^9Hz and 10^{18}Hz , respectively) with aligned ($\theta_{\text{obs}} = 0$) and misaligned ($\theta_{\text{obs}} = 0.16\text{rad}$) viewing angles. The overall agreement is good: `afterglowpy` captures the salient features of both aligned and misaligned light

curves including the jet break, spectral shape, and transition to the Sedov phase. The relative error is less than 50% before the onset of spreading.

TODO: FINISH THIS SECTION.

`afterglowpy` is available on PyPI and may be installed with pip. The source code is open and available at <https://github.com/geoffryan/afterglowpy>.

4. STRUCTURED JET LIGHT CURVES

To fully characterize the light curves of structured jets we use `afterglowpy` to construct light curves exploring dependence on jet structure model, viewing angle θ_{obs} , opening angle θ_c , and synchrotron regime.

We find the light curves of structured jets show two modes of behaviour, depending on whether the observer is *aligned* ($\theta_{\text{obs}} < \theta_c$) or *misaligned* ($\theta_{\text{obs}} > \theta_c$). In the *aligned* case, the light curves follow the standard on-axis top hat behaviour modified slightly for non-zero viewing angle. There is little to distinguish between different structure $E(\theta)$, and the light curve is well-approximated by a broken power law with characteristic break times. The *misaligned* light curve also may present as a broken power law, but with closure relations explicitly dependent on viewing angle and jet angular structure.

We discuss aligned evolution in detail in Section 4.1 and misaligned in Section 4.2. In both cases the transition between phases of evolution depends on the effective solid angle $\Delta\Omega$ of the patch of blast wave dominating the emission. The size of this patch tends to scale with the Lorentz factor γ of the dominant region as:

$$\Delta\Omega = \gamma^{-s_\Omega} . \quad (10)$$

The parameter s_Ω controls the growth rate of the visible patch, and is typically between 0 and 2.

4.1. Aligned Evolution: $\theta_{\text{obs}} \lesssim \theta_c$

The aligned light curve of a structured jet is essentially identical to that of a standard top-hat viewed within the jet cone. (CITE Panaitescu & Kumar). The relativistic afterglow is comprised of three phases, *pre-jet break*, *transition*, and *post-jet break*. These are well described in the literature and are briefly reviewed here.

Pre-jet break — At early times the flux is dominated by the small patch of material whose emission is beamed towards the observer of angular width $\psi = |\theta - \theta_{\text{obs}}| \sim \gamma^{-1}$. This patch is within the $\theta < \theta_c$ region where $E(\theta) \approx E_0$ and the structure plays a sub-dominant role. The angular size of the visible patch grows with $s_\Omega = 2$. Closure relations and scalings of the standard on-axis top-hat apply. (CITE Granot and Sari)

Transition — When $\gamma^{-1} \sim \theta_c - \theta_{\text{obs}}$ the near edge of the jet comes in to view. Material outside θ_c is less

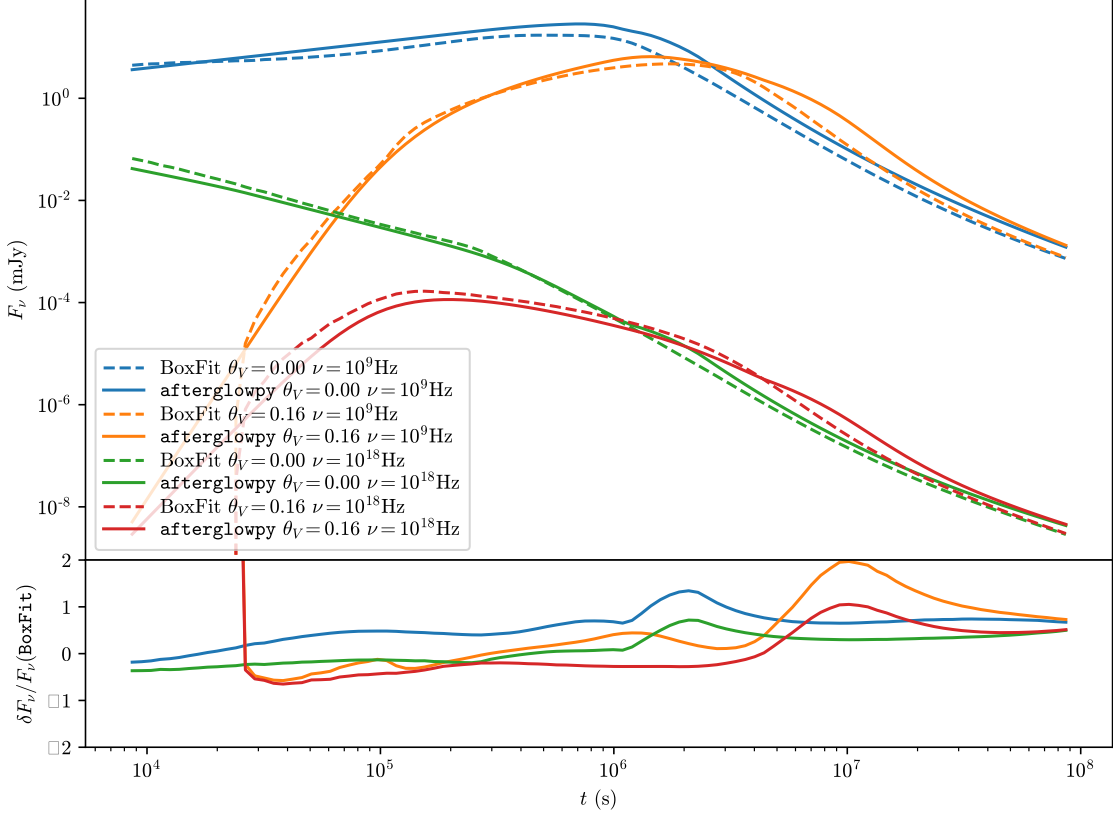


Figure 2. Top Panel: Comparison between top hat jet light curves from `afterglowpy` (solid lines) and `BoxFit` (dashed lines). Bottom Panel: fraction difference between `afterglowpy` and `BoxFit` light curves. Four representative light curves are shown: radio on-axis ($\theta_{\text{obs}} = 0$, $\nu = 10^9 \text{ Hz}$, blue), radio off-axis ($\theta_{\text{obs}} = 0.16 \text{ rad}$, $\nu = 10^9 \text{ Hz}$, orange), x-ray on-axis ($\theta_{\text{obs}} = 0$, $\nu = 10^{18} \text{ Hz}$, green), and x-ray off-axis ($\theta_{\text{obs}} = 0.16 \text{ rad}$, $\nu = 10^{18} \text{ Hz}$, red). Remaining parameters are shared: $\theta_c = 0.1 \text{ rad}$, $E_{\text{iso}} = 10^{52} \text{ erg}$, $E_{\text{iso}} = 10^{52} \text{ erg}$, $n_0 = 10^{-3} \text{ cm}^{-3}$, $p = 2.2$, $\varepsilon_e = 10^{-1}$, $\varepsilon_B = 10^{-2}$, $d_L = 3.09 \times 10^{26} \text{ cm}$, $z = 0.028$.

energetic and contributes sub-dominantly to the afterglow emission. The effective visible patch grows more slowly, $s_\Omega \lesssim 2$, and the decay of the afterglow steepens slightly. Closure relations and scalings of the standard on-axis top-hat apply only approximately (CITE vanEerten MacFadyen 2010).

Post-jet break — When $\gamma^{-1} \sim \theta_c + \theta_{\text{obs}}$ the far edge of the jet comes in to view and growth of the visible patch ceases, $s_\Omega = 0$. If the blast wave remains relativistic and non-spreading, the slope of the light curve is reduced by $-3/4$ relative to the pre-jet break slope. However, in many circumstances the jet break begins when the blast wave is only trans-relativistic and spreading may have begun. In these cases an analytic treatment of the light curve is more difficult, but numerical simulations and analytic work estimate an additional reduction of “???” over the simple analytic result.

The transition between pre-jet break and post-jet break begins at t_{b-} and completes at t_{b+} , given in the

single shell approximation (see Appendix A) by:

$$t_{b\pm} = \left(\frac{9}{16\pi} \frac{E_0}{n_0 m_p c^5} \right)^{1/3} \left(2 \sin \left(\frac{\theta_c \pm \theta_{\text{obs}}}{2} \right) \right)^{8/3}. \quad (11)$$

It is important to note that when $\theta_{\text{obs}} \neq 0$ the transition period is extended, and the most significant transition in the light curve occurs at t_{b+} , the *jet break*. The jet break occurs, in all jets, when the effective angular size of the visible patch of the jet ceases to increase, that is when $s_\Omega = 0$.

Figure 3 shows the jet break time for on-axis ($\theta_{\text{obs}} = 0$) viewers as a function of θ_c for top-hat, Gaussian, and power law jets calculated with `afterglowpy`. Break times were extracted by fitting the numerical light curve with a two-component broken power law.

Figure 4 shows representative top-hat, Gaussian, and power law jet light curves in the aligned regime. The light curves nearly overlap, demonstrating the similar evolution of all structured jet afterglows when viewed

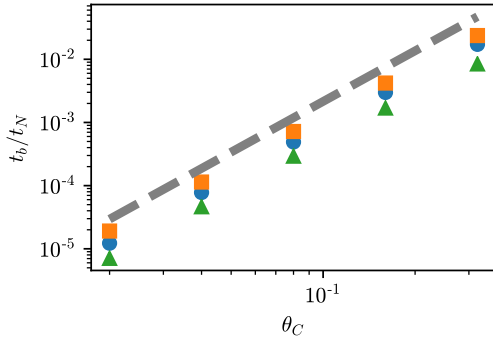


Figure 3. Jet break time for on-axis ($\theta_{\text{obs}} = 0$) observers for top-hat (blue circles), Gaussian (orange squares), and power law (green triangles) jets as a function of θ_c . The dashed grey line is the analytic approximation $t_{\text{b}\pm} = t_N(2 \sin \theta_c/2)^{8/3}$. These particular light curves use $\theta_w = 5\theta_c$, $E_0 = 10^{52}$ erg, $n_0 = 10^{-3}$ cm $^{-3}$, $p = 2.2$, $\varepsilon_e = 10^{-1}$, and $\varepsilon_B = 10^{-4}$.

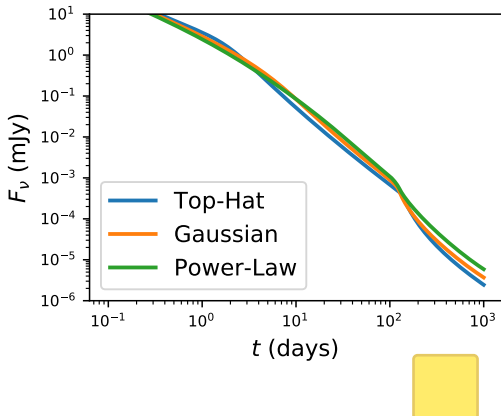


Figure 4. Aligned ($\theta_{\text{obs}} = \theta_c/2$) afterglow light curves for top-hat (blue), Gaussian (orange), and power law (green) jets. When viewed on-axis, jets containing angular structure are very difficult to distinguish from top-hats. The transition phase marking the onset of the jet break begins at $t_{\text{b}-} \sim 3$ days with a shallow break and ends sharply at $t_{\text{b}+} \sim 100$ days. These particular light curves use $\theta_c = 0.1$ rad, $\theta_w = 0.4$ rad, $E_0 = 10^{52}$ erg, $n_0 = 10^{-2}$ cm $^{-3}$, $p = 2.2$, $\varepsilon_e = 10^{-1}$, $\varepsilon_B = 10^{-3}$, and $d_L = 40$ Mpc.

within the jet core. Although we expect all afterglow blast waves to contain angular structure, the simple top-hat jet model is sufficient for aligned viewing.

The relativistic stages of evolution are followed by a Newtonian phase ($t > 200$ days in Figure 4) when the decelerating blast wave becomes non-relativistic, spreads sonically, and approaches a Sedov-Taylor solution. We do not address the Newtonian phase of evolution in this work.

4.2. Misaligned Evolution: $\theta_{\text{obs}} \gtrsim \theta_c$

When viewed at angles larger than θ_c the gradient $E'(\theta)$ over the visible patch becomes non-negligible. To observers this energy gradient presents itself as a slowly rising or decaying afterglow light curve. The relativistic afterglow is comprised of two or three phases depending on whether the observer lies within the truncation angle, *far off-axis, structured, and post-jet break*.

Far off-axis — If the viewer lies outside the truncation angle, $\theta_{\text{obs}} > \theta_w$, then at early times the entire blast wave surface is off-axis and all emission is beaming suppressed. This greatly reduces the early flux and leads to a dim but steeply rising light curve as the blast wave decelerates. Emission is dominated by material on the edge nearest the observer and the angular size of the visible patch is constant in time. This phase ends at t_w when $\gamma^{-1} \sim \theta_{\text{obs}} - \theta_w$. If $\theta_{\text{obs}} < \theta_w$ this phase is entirely absent. Table 1 gives the temporal power law slope of the light curve in this phase. These slopes are derived in Appendix A.

Structured — The structured phase is the direct result of the energy gradient along the observer’s line of site. The usual (pre-jet break) decay is compensated for by regions of higher energy continuously coming into view as the jet decelerates. These new contributions to the emission slow the decay and can even cause the observed flux to increase with time.

This phase begins at observer time t_w , once the blast wave is decelerating and the observer is within the beaming cone of any part of the emitting surface. It ends at observer time t_b , when the jet core has become fully visible. These times are:

$$t_w = \left(\frac{9}{16\pi} \frac{E(\theta_w)}{n_0 m_p c^5} \right)^{1/3} \left(2 \sin \left(\frac{\theta_{\text{obs}} - \theta_w}{2} \right) \right)^{8/3}, \quad (12)$$

$$t_b = \left(\frac{9}{16\pi} \frac{E_0}{n_0 m_p c^5} \right)^{1/3} \left(2 \sin \left(\frac{\theta_{\text{obs}}}{2} \right) \right)^{8/3}. \quad (13)$$

Figure 5 shows the light curve of a Gaussian structured jet along with the emissions from different latitudes. The part of the blast wave dominating the emission tracks from the high latitude wings $\theta \approx \theta_w$ to the core $\theta \approx 0$. The angular size of the visible patch grows approximately as $\gamma^{-1.0}$. (NEED PLOT?)

During the structured phase, the afterglow temporal spectral slope which depends on the parameter $g(\theta^*)$, where θ^* is the latitude of material dominating the emission:

$$g(\theta^*) \equiv -2 \tan \left(\frac{\theta_{\text{obs}} - \theta^*}{2} \right) \frac{d \log E}{d \theta}. \quad (14)$$

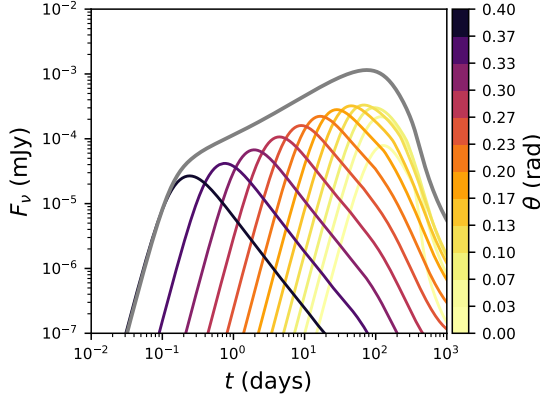


Figure 5. A Gaussian structured jet, decomposed into emission from different latitudes θ . The off-axis, structured, and post-jet break phases are all clearly visible. The structured phase is the result of the brightest point of the blast-wave tracking from the wings ($\theta = \theta_w$) to the jet core ($\theta = \theta_c$).

The temporal and spectral slopes for various regimes are given in Table 1. The derivation of the closure relations, t_w , and t_b are given in Appendix A.

The g parameter evolves with time as θ^* sweeps from the jet edge to the core. This produces deviations in the light curve from a pure power law. However, we find ultimately these deviations are not too large and the average slope is well approximated by $g_{\text{eff}} = g(\theta_{\text{obs}}/2)$. For the power law and Gaussian jet models this gives:

$$g_{\text{eff}} = \frac{\theta_{\text{obs}}^2}{4\theta_c^2} \quad \text{Gaussian ,} \quad (15)$$

$$g_{\text{eff}} = \frac{b\theta_{\text{obs}}^2}{4\theta_c^2 + \theta_{\text{obs}}^2} \quad \text{power law .} \quad (16)$$

These values may be used in Table 1 for an approximate power law model of a structured jet with an appropriate viewing angle dependent temporal evolution. These analytic results are in agreement with previous work on structured jets (CITE ROSSI) and the trans-relativistic numerical model described in Section 3.

In the structured phase, the temporal slope depends directly on the ratio $\theta_{\text{obs}}/\theta_c$. Therefore any measurement of the effective power law slope of an afterglow light curve in the structured phase can be used to measure this parameter.

Post-jet break — Once the entire jet is visible (ie. the observer is within the beaming cone of the entire jet) the visible patch no longer grows and emission is dominated by the decelerating core. This phase follows exactly the post-jet break scalings of the aligned case, except with a much delayed break time t_b .

Figures 6 and 7 display afterglows from the fiducial models in the misaligned regime at $\theta_{\text{obs}} = 2\theta_c$ and $\theta_{\text{obs}} = 6\theta_c$ respectively. At the moderate $2\theta_c$ viewing angle both

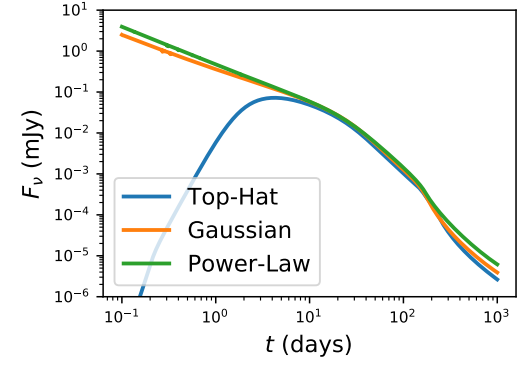


Figure 6. As Figure 4 but $\theta_{\text{obs}} = 2\theta_c$. The top-hat jet (with opening angle θ_c) begins in the off-axis phase. The Gaussian and power law jets begin in the structured phase as $\theta_{\text{obs}} < \theta_w$. All three models enter similar post-jet break phases.

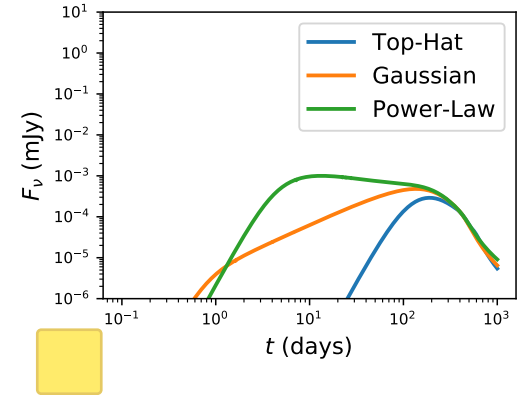


Figure 7. As Figure 4 but $\theta_{\text{obs}} = 6\theta_c$. All three models exhibit off-axis, structured, and post-jet break phases of evolution. At larger opening angles the difference between structured models is more evident.

structured models exhibit similar decaying light curves with slopes somewhat shallower than the aligned case. In this case $\theta_{\text{obs}} < \theta_w$ so neither model exhibits an off-axis phase. The similar temporal evolution is easy to understand as at this angle both models have $g_{\text{eff}} = 1$ and hence approximately equal power law slopes in the structured phase. At late times as more of the jet comes in to view the difference between all three models becomes negligible.

At the larger $6\theta_c$ viewing angle all three models exhibit off-axis, structured, and post-jet break phases of the afterglow. The different t_w between the Gaussian and power law models is due to the different $E(\theta_w)$ of the two models. In the structured phase the Gaussian shows a rising light curve with slope 1 due to the large $g_{\text{eff}} = 9$. The power law meanwhile has a smaller g_{eff}

Table 1. Structured jet temporal and spectral slopes: $F_\nu \propto t_{\text{obs}}^{-\alpha} \nu^{-\beta}$. See Equations (14) and (16) for the definition and effective values of g .

Regime	Label	$\alpha_{\text{off-axis}}$	α_{struct}	$\alpha_{\text{struct,max}}$	$\alpha_{\text{post,analytic}}$	β
$\nu < \nu_m < \nu_c$	D	7	$\frac{1+3g}{8+g}$	3	-1/4	1/3
$\nu_m < \nu < \nu_c$	G	$15/2 - 3p/2$	$\frac{3-6p+3g}{8+g}$	3	$-3p/4$	$(1-p)/2$
$\nu < \nu_c < \nu_m$	E	$17/3$	$\frac{-5/3+11g/3}{8+g}$	11/3	$-7/12$	1/3
$\nu_c < \nu < \nu_m$	F	$13/2$	$\frac{-5+2g}{8+g}$	2	-1	-1/2
$\nu_c < \nu_m < \nu$	H	$8 - 3p/2$	$\frac{1-6p+2g}{8+g}$	2	$-(3p+1)/4$	$-p/2$

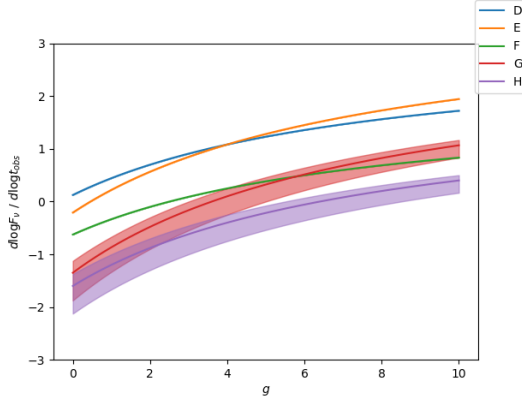


Figure 8. Temporal slopes for the off-axis structured jet as a function of the structure parameter g for the synchrotron spectral regimes D (blue, narrow), E (orange, narrow), F (green, narrow), G (red, wide), and H (purple, wide). The width of the G and H bands shows the dependency on p , the upper curves for $p = 2$ and the lower for $p = 3$. The temporal power law slope of a structured jet afterglow increases with g in all spectral regimes.

of 9/5, giving rise to a very shallow decay. As at the other viewing angles, once the entire jet is visible at t_b all models follow similar post-jet break evolutions.

Figure 8 shows the structured phase power law temporal slope as a function of g for spectral regimes D–H. In the G and H regimes the spectral slope is a function of p , this dependence carries over into the temporal slope as well. The temporal slope is an increasing function of g in all regimes. At sufficiently large g all regimes exhibit rising light curves, the specific g at which the light curve begins to rise is regime dependent.

5. REFRESHED SHOCKS — FAST TAILS AND SPHERICAL COCOONS

An alternative mechanism to produce slow decays or rises in afterglow light curves is the *refreshed shock*, where velocity stratification of the ejecta causes a prolonged period of energy injection in the afterglow. This material may be a tail of fast outflowing ejecta or ejecta

material accelerated through interaction with a possibly choked jet (e.g. a cocoon). (CITE Mooley, Hotokezaka, Nakar&Piran, etc). In either case, slow material initially coasting behind the shock is gradually incorporated into the blast wave as it decelerates, “refreshing” the shock. This mechanism was first proposed as an energy injection scenario (CITE), and was proposed as the mechanism behind the GW170817A afterglow in the choked-jet scenario. (CITE Mooley, Hotokezaka, etc).

In the simplest case the visible part of the blast wave is assumed to be quasi-spherical. The velocity distribution of material behind the blast wave is specified by $E_>(u)$, the energy of all material in the ejecta with four-velocity greater than u . This is typically taken to be a power law in u within the finite domain $[u_{\min}, u_{\max}]$:

$$E_>(u) = E_r u^{-k}, \quad (17)$$

where $u \in (u_{\min}, u_{\max})$ is the dimensionless four-velocity, $k > 0$ is the power law index, and E_r is a normalization factor. The mass ejected with velocity u_{\max} is M_{ej} .

A blast wave will have an initial coasting period before sweeping up enough mass in the ambient medium to begin deceleration and be subject to refreshed shocks. The transition between coasting and decelerating occurs in the bursters frame at t_{dec} . The shock refreshment ends when the blast wave decelerates past u_{\min} , in the observers frame at t_{\min} . In the single shell model with trans-relativistic equation of state used here, these times are:

$$t_{\text{dec}} = \left(\frac{9}{4\pi} \frac{M_{\text{ej}}}{n_0 m_p c^3} \frac{\gamma_{\max}^2}{\beta_{\max}^3 (\gamma_{\max} + 1)(4u_{\max}^2 + 3)} \right)^{1/3}, \quad (18)$$

$$t_{\min} = \left(\frac{9}{16\pi} \frac{E_r}{n_0 m_p c^5} \right)^{1/3} u_{\min}^{-8/3}. \quad (19)$$

Equation (19) assumes $E_r \gg M_{\text{ej}} c^2$. The temporal and spectral slopes in this mechanism depend on the energy distribution index k and are given in Table 2. Figure 9

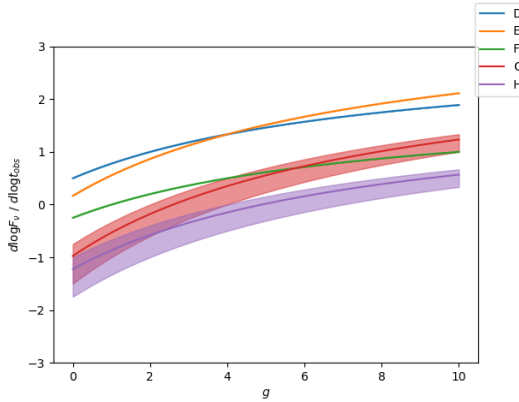


Figure 9. The temporal power law slope of the spherical refreshed-shock afterglow light curve as a function of k . Otherwise as Figure 8. The temporal power law slope of a structured jet afterglow increases with k in all spectral regimes.

shows the temporal slopes in each spectral regime as a function of k . As in Figure 8 the width of the G and H regimes reflects varying the value of p between two and three. For a derivation see Appendix ??.

6. RELATION TO ENERGY INJECTION MODELS

The light curves of both the misaligned angularly structured jet and refreshed shock models can be understood in terms of general energy injection mechanisms, parameterized as an additional power L delivered to the blast wave. This power is typically taken to decay in time as a power law, $L \propto t^{-q}$, with $q \in [0, 1]$.

The mapping between energy injection and refreshed shocks was done by Zhang et al. (2006). That work specifies the index s of the mass distribution $M_{>u} \propto u^{-s}$, which is related simply to the index k by $k = s - 1$. Under this mapping the closure relations in Table 1 are equivalent to those in Zhang et al. (2006) and the model can be seen as equivalent to a energy injection model with $q = (8 - 2k)/(8 + k)$.

Misaligned structured jets do not map as neatly onto energy injection models as the scaling of the visible patch, $s_\Omega = 1.0$, is different than in standard afterglows, $s_\Omega = 2$. Once this change is accounted for, the parameter plays the same role as k , as can be seen by a simple comparison between α_{struct} in Table 1 and α_{refresh} in Table 2. That is, a structured jet light curve is equivalent to a standard energy injection model with:

$$q = (8 - 2g)/(8 + g) \quad (20)$$

$$s_\Omega = 1 \quad (21)$$

Generic closure relations leaving the dependence on s_Ω explicit are presented in Table 3.

7. APPLICATION: GW170817A

We use the electromagnetic afterglow of GW170817A as an example application of both the analytic and numerical structured jet afterglow models.

Figure ?? shows the observations in radio, optical, and x-ray bands of the GW170817A afterglow. No afterglow emission was detected until an x-ray detection by the Chandra observatory nine days after the GW trigger Troja et al. (2017). Further radio, optical, and x-ray observations showed a steady rising light curve with constant power law slope until a peak near day 160. At this point the light curve turned over and began a steep decay that continues to the present (van Eerten et al. 2018).

Interpreting the afterglow as arising from a structured jet allows one to quickly draw the following conclusions:

1. The spectral slope $\beta = 0.585$ (CITE, +uncertainties) throughout the entire evolution, identifying the relevant spectral regime as G : $\nu_m < \nu_{\text{obs}} < \nu_c$, and $p = 2.17$.
2. The initial rising ($\alpha > 0$) light curve with declining spectrum ($\beta < 0$) identify this as a *misaligned* evolution ($\theta_{\text{obs}} > \theta_c$). Aligned jets may only have a rising light curve when viewed at frequencies below the peak frequency, that is when $\beta < 0$.
3. The rising light curve maintains $\alpha = 0.90 \pm 0.06$ (CITE YITL). Using the closure relations from Table 1 we can identify this as the *structured* phase and determine $g_{\text{eff}} = 7.5 \pm 0.4$. If the light curve underwent an *off-axis* phase, it concluded before the afterglow was detected: $t_w < 9\text{d}$. The peak can be identified as the jet-break: $t_b = 164 \pm 12\text{ d}$.
4. In the context of a Gaussian jet, the measurement of g_{eff} leads immediately to $\theta_{\text{obs}}/\theta_c = 5.5 \pm 0.2$.
5. Using the Fong 2015 (CITE Fong 2015) fiducial values of $E_0 \sim 2 \times 10^{51}\text{erg}$ and $n_0 \sim 10^{-2}\text{cm}^{-3}$ we can use the jet break t_b measurement to determine $\theta_{\text{obs}} \approx 0.5 \pm 0.2\text{ rad}$ ($29^\circ \pm 12^\circ$), assuming 1 dex uncertainties on E_0 and n_0 . This is in agreement with the LIGO measurement $\theta_{\text{obs}} \approx 28^\circ \pm 15^\circ$ (assuming the SHoES H_0).
6. The combined measurements of θ_{obs} and $\theta_{\text{obs}}/\theta_c$ then imply $\theta_c \approx 0.09 \pm 0.04\text{ rad}$ ($5^\circ \pm 2^\circ$).

For a more detailed analysis we performed Bayesian parameter estimation utilizing `afterglowpy` and the `emcee` Markov chain Monte Carlo sampler (Foreman-Mackey et al. 2013). We used the light curve data reported in van Eerten et al. (2018) with additional *Hubble Space Telescope* observations reported in Lamb et al.

Table 2. Refreshed shock temporal and spectral slopes: $F_\nu \propto t_{\text{obs}}^{-\alpha} \nu^{-\beta}$. See Equation (17) for the definition of k .

Regime	Label	α_{coast}	α_{refresh}	$\alpha_{\text{refresh,max}}$	α_{post}	β
$\nu < \nu_m < \nu_c$	D	3	$-\frac{4+3k}{8+k}$	-3	-1/2	-1/3
$\nu_m < \nu < \nu_c$	G	3	$-\frac{6+6p-3k}{8+k}$	-3	$3(p-1)/4$	$(p-1)/2$
$\nu < \nu_c < \nu_m$	E	3	$-\frac{4/3+11k/3}{8+k}$	-11/3	-1/6	-1/3
$\nu_c < \nu < \nu_m$	F	3	$\frac{2-2k}{8+k}$	-2	1/4	1/2
$\nu_c < \nu_m < \nu$	H	3	$-\frac{4+6p-2k}{8+k}$	-2	$(3p-2)/4$	$p/2$



Table 3. Generic closure relations for the afterglow of a relativistic blast wave in a homogeneous medium: $F_\nu \propto t_{\text{obs}}^\alpha \nu^\beta$. See Equations (14) and (16) for the definition and effective values of g for misaligned structured jets. Jets aligned with the viewer or without angular structure have $g = 0$. The visible patch of the jet has a solid angle which scales as γ^{-s_Ω} . A uniform relativistic blast wave pre-jet break has $s_\Omega = 2$, a relativistic blast wave with angular structure pre-jet break has $s_\Omega \approx 1$, and a relativistic blast wave post jet-break has $s_\Omega = 0$. For a refreshed-shock model replace g with k , defined in Equation (17).

Regime	Label	α	β
$\nu < \nu_m < \nu_c$	D	$-\frac{-2+3s_\Omega+3g}{8+g}$	1/3
$\nu_m < \nu < \nu_c$	G	$-\frac{-6p+3s_\Omega+3g}{8+g}$	$(1-p)/2$
$\nu < \nu_c < \nu_m$	E	$-\frac{-14/3+3s_\Omega+11g/3}{8+g}$	1/3
$\nu_c < \nu < \nu_m$	F	$-\frac{-8+3s_\Omega+2g}{8+g}$	-1/2
$\nu_c < \nu_m < \nu$	H	$-\frac{-6p-2+3s_\Omega+2g}{8+g}$	$-p/2$

(2019). Reported measurement uncertainties were assumed to be independent and Gaussian, upper limits were treated as observations of zero flux with a 1-sigma Gaussian uncertainty.

We fit both the Gaussian and power law structured jet models, fixing $\xi_N = 1$ and $d_L = 1.23 \times 10^{26}$ cm. The fit parameters, their priors, and their marginalized posteriors are given in Table 4. Both models were run with 300 walkers for 64 000 iterations, discarding the first 16 000 iterations as a burn-in. The viewing angle prior is the posterior found in analysis of the GW170817A gravitational wave signal assuming the value of H_0 reported by the *Planck* collaboration (Abbott et al. 2017; Planck Collaboration et al. 2016; Troja et al. 2018).

Figures 10 and 11 show the one- and two-dimensional marginalized views of the posterior distribution for the Gaussian and power law jet model fits, respectively. Table 4 additionally gives constraints on the total jet

energy E_{tot} and the ratio $\theta_{\text{obs}}/\theta_c$. The parameters E_0 , n_0 , ε_e , and ε_B are only constrained to within an order of magnitude, due partially to the observed radio, optical, and x-ray data all lying on the same synchrotron power-law segment. These parameters are shared between jet models, and are broadly consistent between the two fits with the possible exception of n_0 . The electron energy index p is extremely well constrained by both models, of course, due precisely to the large range of data laying on the same synchrotron segment. The total jet energy in both models is constrained to be on the order 10^{51} erg.

Of most interest are the geometric parameters: the viewing angle θ_{obs} and the jet structure parameters θ_c , θ_w , and b . Encouragingly, the fits agree with the back-of-the-envelope reasoning from the analytic closure relations and break time scalings. Both models constrain θ_{obs} and θ_c reasonably well, but constrain the combination $\theta_{\text{obs}}/\theta_c$ far better. This is very evident by the



Table 4. Parameter estimation priors and marginalized posteriors for the GW170817A afterglow using the `afterglowpy` Gaussian and power law jet models, including viewing angle constraints from LIGO assuming the *Planck* value of H_0 . Given posterior values for each model are the median, 16%, and 84% quantiles. Parameters in the lower section are derived from the posterior distributions of the fit parameters in the upper sections.

Parameter	Unit	Prior Form	Bounds	Gaussian Jet Posterior	Power Law Jet Posterior
θ_{obs}	rad	$\sin \theta_{\text{obs}} \times p_{\text{LIGO}}(\cos \theta_{\text{obs}})$	[0, 0.8]	$0.48^{+0.08}_{-0.09}$	$0.36^{+0.14}_{-0.11}$
$\log_{10} E_0$	erg	uniform	[45, 57]	$52.92^{+0.62}_{-0.49}$	$53.01^{+0.99}_{-0.70}$
θ_c	rad	uniform	$[0.01, \pi/2]$	$0.07^{+0.01}_{-0.01}$	$0.10^{+0.06}_{-0.03}$
θ_w	rad	uniform	$[0.01, 12\theta_c]$	$0.77^{+0.43}_{-0.38}$	$0.18^{+0.07}_{-0.05}$
b	—	uniform	[0, 10]	—	$7.15^{+2.02}_{-1.12}$
$\log_{10} n_0$	cm^{-3}	uniform	$[-10, 10]$	$-1.94^{+0.62}_{-0.65}$	$-2.66^{+1.03}_{-1.11}$
p	—	uniform	[2, 5]	$2.17^{+0.01}_{-0.01}$	$2.17^{+0.01}_{-0.01}$
$\log_{10} \varepsilon_e$	—	uniform	$[-5, 0]$	$-1.24^{+0.48}_{-0.69}$	$-1.30^{+0.66}_{-1.07}$
$\log_{10} \varepsilon_B$	—	uniform	$[-5, 0]$	$-4.32^{+0.72}_{-0.49}$	$-3.84^{+1.01}_{-0.80}$
$\log_{10} E_{\text{tot}}$	erg	—	—	$50.61^{+0.58}_{-0.44}$	$50.85^{+0.93}_{-0.63}$
$\theta_{\text{obs}}/\theta_c$	—	—	—	$6.76^{+0.21}_{-0.21}$	$3.78^{+0.58}_{-0.84}$

corresponding map of the posterior in Figures 10 and 11, which clearly displays a preferred linear relationship between θ_{obs} and θ_c . This is the manifestation of the structured jet closure relations with $g \approx g_{\text{eff}}(\theta_{\text{obs}}/\theta_c)$. The looser constraint on $\theta_{\text{obs}}/\theta_c$ in the power law jet comes from the additional freedom of the b parameter, which has an effect on g_{eff} in that model (see Equation (16)). The truncation angle θ_w is essentially unconstrained in the Gaussian fit as a far off-axis phase was not observed. In the power law fit, however, θ_w is constrained to be quite narrow so as to avoid the early bright wings.

Despite the tight constraints each model gives on θ_{obs} , θ_c , and especially $\theta_{\text{obs}}/\theta_c$, the resulting posteriors are incompatible with each other. The median and 68% uncertainties in Table 4 display only a mild tension in θ_{obs} and θ_c themselves, but a very large discrepancy in $\theta_{\text{obs}}/\theta_c$. This is, of course, due to the very different energy profiles $E(\theta)$ in each model. Both models can easily accommodate a rising light curve $F_\nu \sim t^{0.9}$, that is produce an effective structure parameter $g_{\text{eff}} = 7.5$, but do so using very different geometries.

8. DISCUSSION

8.1. Inferring θ_{obs} and $E(\theta)$

Information about the viewing angle and jet structure is clearly encoded within misaligned afterglow light curves, primarily through the temporal slope α during the structured phase. This parameter alone, however, does not uniquely identify a particular structure model or observer inclination. When trying to infer informa-

tion about a particular afterglow, there is a massive degeneracy between $E(\theta)$ and θ_{obs} .

This degeneracy is a blessing and a curse. The presence of an extended slowly decaying or rising afterglow is a largely model independent prediction of misaligned viewing and the presence of non-trivial jet structure. Unfortunately, this same model independence makes it very difficult to distinguish between jet structure profiles, leaving both $E(\theta)$ and θ_{obs} uncertain.

There are at least two ways of easing this degeneracy: incorporating data other than the afterglow light curve itself and looking at population-level statistics. Utilizing posteriors from the gravitational wave signal or fitting the VLBI observations of superluminal apparent motion can greatly improve constraints on θ_{obs} (Troja et al. 2018; Hotokezaka et al. 2018; Ghirlanda et al. 2019). Since the afterglow presumably provides good constraints on g_{eff} (via α), improved knowledge of θ_{obs} immediately improves knowledge of θ_c , b , and any other parameters relevant to $E(\theta)$. In some cases this may rule out a particular $E(\theta)$ entirely by pushing the relevant parameters to extreme values, for instance it is hard (but not impossible) to reconcile the observations of GW170817A with a power law jet with $b = 2$.

In the future, it may be possible to attack the question of determining $E(\theta)$ at the population level. Figure 12 shows the structure parameter g as a function of $\theta_{\text{obs}}/\theta_c$ for several jet models, as well as the inferred value from GW170817A. If all short GRB jets share a jet profile shape, they should trace out a single curve in this space. As more misaligned afterglows are observed, measurements of g can populate this diagram

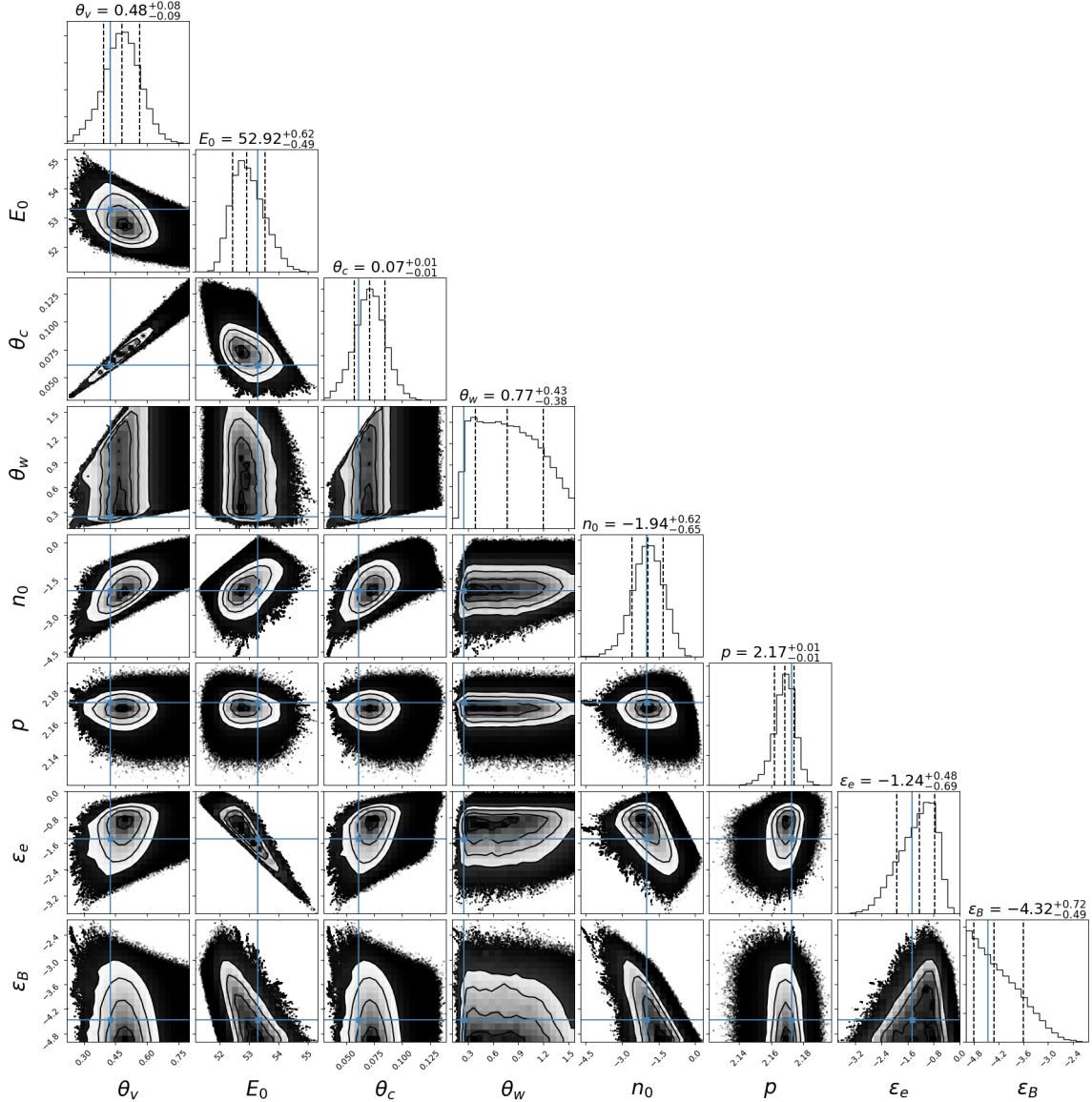


Figure 10. Views of the posterior parameter distribution for a Gaussian jet fit to the GW170817A afterglow. The diagonal contains one-dimensional marginalized posteriors for each fit parameter, while the off-diagonal plots contain two-dimensional marginalized posteriors over all but the two corresponding parameters.

and potentially rule out models (such as potentially the $b = 2$ power law). Model-independent constraints on $\theta_{\text{obs}}/\theta_c$ will greatly aid this procedure. Moreover, each structure model should predict a different observed distribution of g , depending on the shape of the $g(\theta_{\text{obs}}/\theta_c)$ curve and the detectability of each burst. With sufficient observations of g alone and understanding of the observational biases, it may be possible to infer the underlying $g(\theta_{\text{obs}}/\theta_c)$ curve and $E(\theta)$ itself.

8.2. Comparison With Other GW170817A Analyses

Many groups have used structured jet models to analyze the afterglow of GW170817A, among the most recent with comparable models are Hotokezaka et al.

(2018); Ghirlanda et al. (2019); Lamb et al. (2019); Wu & MacFadyen (2018). Of these, Hotokezaka et al. (2018); Ghirlanda et al. (2019); Lamb et al. (2019) use semi-analytic methods similar to the present work to construct afterglow light curves, while Wu & MacFadyen (2018) utilizes analytic scaling relations and a template bank constructed from numerical simulations. Additionally, Hotokezaka et al. (2018); Ghirlanda et al. (2019) include constraints from the VLBI measurements of the GW170817A radio centroid's apparent superluminal motion.

TODO: INCLUDE BRIEF COMPARISON TO EACH. NOTE DIFFERENT MODELS PRODUCE SAME LIGHT CURVE, STRONG EFFECT OF VLBI.



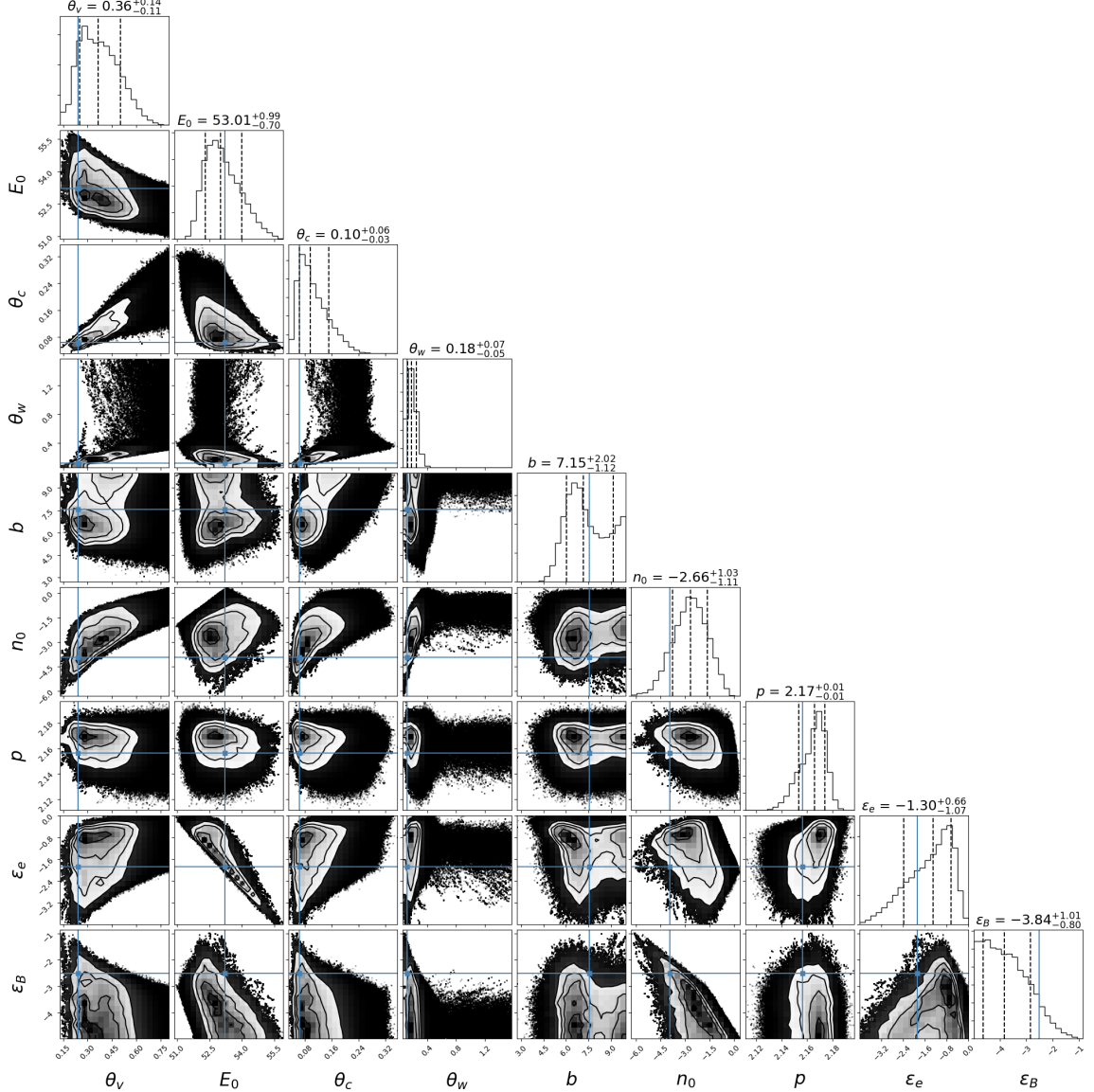


Figure 11. Views of the posterior parameter distribution for a power law jet fit to the GW170817A afterglow. The diagonal contains one-dimensional marginalized posteriors for each fit parameter, while the off-diagonal plots contain two-dimensional maps of the posterior marginalized over all but the two corresponding parameters.

8.3. O3 And Beyond

In the coming years there will be more GW170817A-like events, although perhaps few with as extensive followup campaigns. Since many of these events may be faint and distant, it will be important to leverage as much information from the afterglow light curve as possible. As shown here, and evidenced by the diversity of models that have “fit” the GW170817A afterglow, there is a large degeneracy between viewing angle and jet structure profile. To make robust inferences about these events, several flexible jet models must be included in the analysis.

We hope `afterglowy` and similar products will aid these analyses in the future.

9. SUMMARY

We have constructed flexible models for the electromagnetic afterglows of angularly structured relativistic jets. Through analytic approximations we can identify the basic phases of the structured afterglow light curve, determining formulae for the characteristic break time scales and closure relations. We find the closure relations depend on a single parameter we call g relating to the jet structure and viewing angle. Measurements of g itself are model independent, but relating it back to physical parameters of the jet is not.

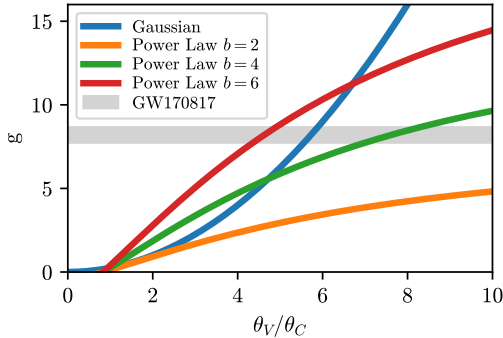


Figure 12. Structure parameter g as a function of $\theta_{\text{obs}}/\theta_c$ for different structured jet models: Gaussian (blue), $b = 2$ power law (orange), $b = 4$ power law (green), and $b = 6$ power law (red). The inferred value $g = 8.2 \pm 0.5$ for GW170817A is shown in as the grey band.

We also constructed a numerical model of the afterglows of structured jets, implemented in the public Python package `afterglowpy`. `afterglowpy` computes afterglow light curves on the fly utilizing semi-analytic approximations to the jet evolution and synchrotron emission, taking into account relativistic beaming, the equal time of arrival surface, jet angular structure, trans-relativistic evolution, and jet spreading. It is fast enough to be incorporated in MCMC parameter estimation routines. Fitting the GW170817A afterglow with multiple `afterglowpy` models reveals the degeneracy between jet structure and viewing angle.

APPENDIX

A. DERIVATION OF THE OFF-AXIS JET EQUATIONS

The *structured jet* model is a generalization of the simple top hat jet where the energy and Lorentz factor vary with the polar angle. The light curves of structured jets display more complex behavior than top hats, which we can understand through some simple analytic relationships.

Firstly, the complex behavior of a structured jet is due to relativistic beaming enhancing the jet emission at different angles as a function of time. Once the jet becomes non-relativistic this effect is suppressed and the entire jet comes into view. As such we will focus on the emission when the jet remains relativistic, the late-time behavior is the same as any Newtonian jet of comparable total energy. Numerical simulations and analytic considerations have demonstrated that jet spreading does not begin in earnest until the blast wave approaches sub relativistic velocity so we will also neglect the effects of spreading and assume each sector of the jet evolves independently. Lastly, we will assume when each sector of the blast wave is visible it is in the deceleration regime. In this phase of evolution the blast wave Lorentz factor evolves according to:

$$\gamma(t; \theta) \propto \sqrt{\frac{E(\theta)}{n_0}} t^{-3/2}. \quad (\text{A1})$$

In the above γ is the Lorentz factor of the shocked fluid at an angle θ from the jet axis at lab time (in the burster frame) t . The blast wave expands into a medium of constant density n_0 and has an angularly dependent isotropic-equivalent energy $E(\theta)$. The forward shock is at a position $R(t; \theta)$, and moves at a speed $\beta_s = (1 - \gamma_s^{-2})^{1/2}$, where $\gamma_s^2 = 2\gamma^2$ is the Lorentz factor of the shock. Assuming $\gamma \gg 1$ gives:

$$R(t; \theta) = ct \left(1 - \frac{1}{16\gamma^2(t; \theta)} \right). \quad (\text{A2})$$

We denote the angle between the viewer and a particular jet sector as ψ and its cosine and $\mu = \cos \psi$. Photons emitted at time from a sector of the blast wave at time t will be seen by the observer at t_{obs} :

$$t_{\text{obs}} = t - \frac{\mu}{c} R(t; \theta) = (1 - \mu)t + \frac{\mu}{16} \frac{t}{\gamma^2(t; \theta)} \quad (\text{A3})$$

The observed flux depends on the luminosity distance d_L , viewing angle θ_{obs} , and rest-frame emissivity $\varepsilon'_{\nu'}$. The Doppler factor is $\delta = \gamma^{-1}(1 - \beta\mu)^{-1}$, where $\beta = (1 - \gamma^{-2})^{1/2}$ is the fluid three velocity. The observed flux can then be expressed as a volume integral, where the integrand is evaluated at the time t corresponding to t_{obs} and position \mathbf{r} .

$$F_{\nu}(t_{\text{obs}}, \nu_{\text{obs}}) = \frac{1}{4\pi d_L^2} \int d^3 \mathbf{r} \delta^2 \varepsilon'_{\nu'} . \quad (\text{A4})$$

Table 5. Dependence of $\varepsilon'_{\nu'} \propto \gamma^{s_1} t^{s_2} \nu'^{\beta}$ in various spectral regimes.

Regime	s_1	s_2	β
$\nu' < \nu'_m < \nu'_c$	1	0	1/3
$\nu'_m < \nu' < \nu'_c$	(3p + 1)/2	0	(1 - p)/2
$\nu'_m < \nu'_c < \nu'$	3p/2	-1	-p/2
$\nu' < \nu'_c < \nu'_m$	7/3	2/3	1/3
$\nu'_c < \nu' < \nu'_m$	3/2	-1	-1/2
$\nu'_c < \nu'_m < \nu'$	3p/2	-1	-p/2

The blast wave emits from a region of width $\Delta R \propto \delta_s \gamma_s \gamma^{-2} R$ where δ_s is the Doppler factor associated with the shock Lorentz factor γ_s . At a given observer time, the emission will be dominated by a region of (rest-frame) angular size $\Delta\Omega$. The flux can then be approximated as:

$$F_{\nu}(t_{\text{obs}}, \nu_{\text{obs}}) \propto R^2 \Delta R \Delta\Omega \delta^2 \varepsilon'_{\nu'} \propto \Delta\Omega t^3 \gamma^{-2} \gamma_s \delta_s \delta^2 \varepsilon'_{\nu'} \quad (\text{A5})$$

. The emissivity $\varepsilon'_{\nu'}$ depends on the fluid Lorentz factor, the frequency ν_{obs} , and numerous (constant) microphysical parameters. We parameterize the dynamic dependence as $\varepsilon'_{\nu'} \propto \gamma^{s_1} t^{s_2} \nu'^{\beta} = t^{s_2} \gamma^{s_1} \delta^{-\beta} \nu_{\text{obs}}^{\beta}$. The values of s_1 , s_2 , and β in synchrotron regimes are given in Table 5. This leads to a flux of:

$$F_{\nu} \propto \Delta\Omega t^{3+s_2} \gamma^{-1+s_1} \delta_s \delta^{2-\beta} \nu_{\text{obs}}^{\beta}. \quad (\text{A6})$$

The Doppler factor depends on the fluid Lorentz factor and whether the material is on-axis. The on/off axis boundary occurs at $\gamma^{-1} \approx \sin \psi$ (ie. $\beta \approx \mu$). One can write:

$$\delta = \begin{cases} \frac{1}{2} \gamma^{-1} \sin^{-2} \psi / 2, & \text{if } \gamma \gg 1 \text{ and } \sin \psi \gg \gamma^{-1} \text{ (off-axis)} \\ 2\gamma, & \text{if } \gamma \gg 1 \text{ and } \sin \psi \ll \gamma^{-1} \text{ (on-axis)} \\ 1 & \text{if } \beta \ll 1 \text{ (non-relativistic)} \end{cases}. \quad (\text{A7})$$

The observer time can be similarly simplified in both limits:

$$t_{\text{obs}} = \begin{cases} \frac{1}{2} \psi^2 t, & \text{if } \sin \psi \gg \gamma^{-1} \text{ (off-axis)} \\ \frac{1}{16} \gamma^{-2} t, & \text{if } \sin \psi \ll \gamma^{-1} \text{ (on-axis)} \end{cases}. \quad (\text{A8})$$

As can the flux:

$$F_{\nu} \propto \begin{cases} \Delta\Omega t^{3+s_2} \gamma^{-4+s_1+\beta} \psi^{-6+2\beta} \nu_{\text{obs}}^{\beta}, & \text{(off-axis)} \\ \Delta\Omega t^{3+s_2} \gamma^{2+s_1-\beta} \nu_{\text{obs}}^{\beta}, & \text{(on-axis)} \end{cases}. \quad (\text{A9})$$

The behavior of the Doppler factor informs the scaling of $\Delta\Omega$. If any part of the jet is on-axis, its emission is enhanced by $\sim \gamma^2$ over the off-axis material and will dominate. An observer for whom the entire jet is off-axis must be situated at some large θ_{obs} , outside the outermost jet material. At early times the entire jet will be beamed off-axis, with emission from the near edge (with the smallest ψ and presumably γ) contributing most to the emission. The absence of any particular angular scale in this regime indicates $\Delta\Omega$ will be roughly constant. For an on-axis observer $\Delta\Omega \sim \sin^2 \psi_{\text{max}} \propto \gamma^{-2}$ until the entire jet is on-axis, at which point $\Delta\Omega$ is again constant. Hence:

$$F_{\nu} \propto \begin{cases} t^{3+s_2} \gamma^{-4+s_1+\beta} \psi^{-6+2\beta} \nu_{\text{obs}}^{\beta}, & \text{(off-axis)} \\ t^{3+s_2} \gamma^{s_1-\beta} \nu_{\text{obs}}^{\beta}, & \text{(on-axis, pre jet break)} \\ t^{3+s_2} \gamma^{2+s_1-\beta} \nu_{\text{obs}}^{\beta}, & \text{(on-axis, post jet break)} \end{cases}. \quad (\text{A10})$$

Finally, for off-axis emission $t \propto t_{\text{obs}}$ and hence $\gamma \propto t_{\text{obs}}^{-3/2}$. For on-axis observers $t_{\text{obs}} \propto \gamma - 2t \propto t^4$, hence $t \propto t_{\text{obs}}^{1/4}$ and $\gamma \propto t_{\text{obs}}^{-3/8}$. Giving finally:

$$F_\nu \propto \begin{cases} t_{\text{obs}}^{9+s_2-3(s_1+\beta)/2} \psi^{-6+2\beta} \nu_{\text{obs}}^\beta, & (\text{off-axis}) \\ t_{\text{obs}}^{(3+s_2)/4+3(-s_1+\beta)/8} \nu_{\text{obs}}^\beta, & (\text{on-axis, pre jet break}) \\ t_{\text{obs}}^{s_2/4+3(-s_1+\beta)/8} \nu_{\text{obs}}^\beta, & (\text{on-axis, post jet break}) \end{cases} . \quad (\text{A11})$$

These formulae capture the standard behavior of top-hat jets, as well as any jet that is *fully* on-axis or off-axis. What they fail to (easily) demonstrate is the behavior of a structured jet which transitions continuously from one state to the other over the course of observation.

B. DERIVATION OF THE STRUCTURED JET EQUATIONS

A jet with a non-trivial angular distribution of energy can exhibit qualitatively different behaviour than a simple top hat, particularly when observed at a significant viewing angle. While the initial off-axis and final on-axis post jet-break evolutions are identical, these are separated by a transition phase where the sector dominating the emission scans over the jet surface. This transition phase begins at the end of the off-axis phase: when a sector of the jet first decelerates to include the observer in its beaming cone. This will necessarily be from the wings/edge of the jet, the material with the lowest Lorentz factor and smallest angle ψ to the observer. As the blastwave decelerates more energetic material from nearer the core will come into view and the high latitude emission will dim. Finally the core of the jet ($\theta = 0$ or $\psi = \theta_{\text{obs}}$) decelerates and becomes visible to the observer. At this point the entire jet is on-axis and evolution continues as in the post jet-break phase.

At each moment during the structure phase the emission is dominated by material that just came on-axis, where $\gamma^{-1} = \sin \psi$. To find the overall behaviour we first determine $t_{\text{obs}}(\psi)$ and $F_\nu(\psi)$ for material whose emission is peaking (coming on-axis). Since the structure phase occurs when motion is still relativistic, we can assume $\gamma \gg 1$ and hence $\sin \psi \ll 1$. In this approximation:

$$\mu \approx 1 - \frac{1}{2} \sin^2 \psi , \quad (\text{B12})$$

$$\delta_s \approx \delta \approx \gamma = \csc \psi . \quad (\text{B13})$$

The material dominating the emission is in the plane between the observer and the jet axis, denoted by $\phi = 0$. Along this line we have $\psi = \theta_{\text{obs}} - \theta$, and can use ψ or θ interchangeably to denote latitude. From Equation (A1) we have $t \propto E(\theta)^{1/3} \gamma^{-2/3}$. Using Equation (A3) and (B12) we find that material at ψ will come on-axis at observer time:

$$t_{\text{obs}}(\psi) = \frac{9}{16} t \sin^2 \psi \propto E(\theta)^{1/3} \sin^{8/3} \psi . \quad (\text{B14})$$

The peak flux from material at ψ can be determined from Equation (A6). Using Equation (B13) and taking $\Delta\Omega \propto \gamma^{-s_3}$ gives an observed flux:

$$F_\nu(\psi) \propto t^{3+s_2} \gamma^{2+s_1-s_3-\beta} \nu_{\text{obs}}^\beta \propto E(\theta)^{1+s_2/3} (\sin \psi)^{-s_1+2s_2/3+s_3+\beta} \nu_{\text{obs}}^\beta . \quad (\text{B15})$$

Equations (B14) and (B15) describe the evolution of the flux in the structure phase in terms of the parameter ψ , which varies from $\min(0, \theta_{\text{obs}} - \theta_w)$ to θ_{obs} . In principle one would like to invert Equation (B14) and substitute into Equation (B15) to obtain $F_\nu(t_{\text{obs}})$ itself. Unfortunately, in general this is impossible to do in closed form because $E(\theta)$ is non-trivial.

We can obtain the temporal power law slope of the light curve by differentiating both Equations (B14) and (B15) with respect to ψ . Noting that $dE/d\psi = -dE/d\theta$ we obtain for the individual derivatives:

$$\frac{d \log t_{\text{obs}}}{d\psi} = \frac{8}{3} \cot \psi - \frac{1}{3} \frac{d \log E}{d\theta} , \quad (\text{B16})$$

$$\frac{d \log F_\nu}{d\psi} = \left(-s_1 + \frac{2}{3} s_2 + s_3 + \beta \right) \cot \psi - \left(1 + \frac{1}{3} s_2 \right) \frac{d \log E}{d\theta} . \quad (\text{B17})$$

Taking the ratio and simplifying gives:

$$\frac{d \log F_\nu}{d \log t_{\text{obs}}}(\psi) = \frac{3\beta - 3s_1 + 2s_2 + 3s_3 + (3+s_2)g(\psi)}{8 + g(\psi)} \quad (\text{B18})$$

$$g(\psi) \equiv -\tan \psi \frac{d \log E}{d\theta} . \quad (\text{B19})$$

The parameter g is directly measurable from the light curve, given the spectral information which fixes β , s_1 , and s_2 .

The full flux scaling equations also require an updated energy and circumburst density scaling. We can obtain the scalings for energy and density from dimensional analysis, following van Eerten & MacFadyen (2012) (specifically, by making use of the fact that the overall flux scalings for the different spectral regimes should obey those presented in table 1 of that paper).

[RED STUFF IS WRONG SOMEHOW] For energy, it follows that (below ν_c)

$$\frac{d \log F}{d \log E} = \frac{d \log F}{d \Psi} \frac{d \Psi}{d \log E} = - \frac{d \log F}{d \Psi} \frac{d \theta}{d \log E} = \left(s_1 - \frac{2}{3} s_2 - s_3 - \beta \right) h(\Psi) + 1 + \frac{1}{3} s_2, \quad (\text{B20})$$

where

$$h(\Psi) \equiv \cot \Psi \frac{d \log E}{d \theta}. \quad (\text{B21})$$

For the density n_0 we have (below ν_c)

$$\frac{d \log F}{d \log n_0} = \frac{2 + s_3}{8} \quad (\text{B22})$$

Altogether, we obtain

$$\begin{aligned} F_D &\propto (1+z)^{(38-5g(\Psi)-9s_3)/3(8+g(\Psi))} \epsilon_e^{-2/3} \epsilon_B^{1/3} n_0^{(6+4g+3s_3)/3(8+g(\Psi))} E_0^{(26-3s_3)/3(8+g(\Psi))} t_{\text{obs}}^{(-2+3s_3+3g(\Psi))/(8+g(\Psi))} \nu^{1/3} \\ F_E &\propto (1+z)^{(46-7g(\Psi)-9s_3)/3(8+g(\Psi))} \epsilon_B^{14+6g(\Psi)+3s_3)/3(8+g(\Psi))} E_0^{(34-3s_3)/3(8+g(\Psi))} t_{\text{obs}}^{(-14+9s_3+11g(\Psi))/(3(8+g(\Psi)))} \nu^{1/3} \\ F_F &\propto (1+z)^{(24-3g(\Psi)-6s_3)/2(8+g(\Psi))} \epsilon_B^{-1/4} n_0^{(-8+3g(\Psi)+4s_3)/4(8+g(\Psi))} E_0^{(8-s_3)/(8+g(\Psi))} t_{\text{obs}}^{(-8+3s_3+2g(\Psi))/(8+g(\Psi))} \nu^{-1/2} \\ F_G &\propto (1+z)^{\frac{(-pg(\Psi)-3g(\Psi)+4p-6s_3+24)}{2(8+g(\Psi))}} \epsilon_e^{p-1} \epsilon_B^{(1+p)/4} n_0^{(g(\Psi)p+5g(\Psi)+4s_3+8)/4(8+g(\Psi))} E_0^{(8+2p-s_3)/(8+g(\Psi))} t_{\text{obs}}^{3(-2p+s_3+g(\Psi))/(8+g(\Psi))} \nu^{(1-p)/2} \\ F_H &\propto (1+z)^{\frac{(-pg(\Psi)-2g(\Psi)+4p-6s_3+20)}{2(8+g(\Psi))}} \epsilon_e^{p-1} \epsilon_B^{(p-2)/4} n_0^{(g(\Psi)p+2g(\Psi)+4s_3-8)/4(8+g(\Psi))} E_0^{(6+2p-s_3)/(8+g(\Psi))} t_{\text{obs}}^{(-6p-2+3s_3+2g(\Psi))/(8+g(\Psi))} \nu^{-p/2} \\ \nu_m &\propto (1+z)^{\frac{4-g(\Psi)}{8+g(\Psi)}} \epsilon_e^2 \epsilon_B^{1/2} n_0^{g(\Psi)/(16+2g(\Psi))} E_0^{4/(8+g(\Psi))} t_{\text{obs}}^{-12/(8+g(\Psi))} \\ \nu_c &\propto (1+z)^{\frac{-4+g(\Psi)}{8+g(\Psi)}} \epsilon_B^{-3/2} n_0^{-(3g(\Psi)+16)/2(8+g(\Psi))} E_0^{-4/(8+g(\Psi))} t_{\text{obs}}^{-2(2+g(\Psi))/(8+g(\Psi))} \\ F_{\text{peak}} &\propto (1+z)^{\frac{14-2g(\Psi)-3s_3}{8+g(\Psi)}} \epsilon_B^{1/2} n_0^{(4+3g(\Psi)+2s_3)/2(8+g(\Psi))} E_0^{(10-s_3)/(8+g(\Psi))} t_{\text{obs}}^{3(-2+s_3+g(\Psi))/(8+g(\Psi))} \end{aligned} \quad (\text{B23})$$

C. SHOCK JUMP CONDITIONS AND SYNCHROTRON PARAMETERS

Table 6 lists the necessary quantities for calculating synchrotron emission from a forward shock. Asymptotic expressions are given in the ultra-relativistic and non-relativistic limits. The synchrotron emissivity in the fluid rest frame is:

$$\varepsilon'_{\nu'} = \varepsilon_P \times \begin{cases} (\nu'/\nu_m)^{1/3} & \text{if } \nu' < \nu_m < \nu_c \\ (\nu'/\nu_m)^{(1-p)/2} & \text{if } \nu_m < \nu' < \nu_c \\ (\nu_c/\nu_m)^{(1-p)/2} (\nu'/\nu_c)^{-p/2} & \text{if } \nu_m < \nu_c < \nu' \\ (\nu'/\nu_c)^{1/3} & \text{if } \nu' < \nu_c < \nu_m \\ (\nu'/\nu_c)^{-1/2} & \text{if } \nu_c < \nu' < \nu_m \\ (\nu_m/\nu_c)^{-1/2} (\nu'/\nu_m)^{-p/2} & \text{if } \nu_c < \nu_m < \nu' \end{cases} \quad (\text{C24})$$

REFERENCES

- Abbott, B. P., Abbott, R., Abbott, T. D., et al. 2017, Nature, 551, 85, doi: [10.1038/nature24471](https://doi.org/10.1038/nature24471)
- Aloy, M. A., Janka, H.-T., & Müller, E. 2005, A&A, 436, 273, doi: [10.1051/0004-6361:20041865](https://doi.org/10.1051/0004-6361:20041865)
- Duffell, P. C., & Laskar, T. 2018, ApJ, 865, 94, doi: [10.3847/1538-4357/aadb9c](https://doi.org/10.3847/1538-4357/aadb9c)
- Duffell, P. C., & MacFadyen, A. I. 2013, ApJL, 776, L9, doi: [10.1088/2041-8205/776/1/L9](https://doi.org/10.1088/2041-8205/776/1/L9)
- Foreman-Mackey, D., Hogg, D. W., Lang, D., & Goodman, J. 2013, PASP, 125, 306, doi: [10.1086/670067](https://doi.org/10.1086/670067)
- Ghirlanda, G., Salafia, O. S., Paragi, Z., et al. 2019, Science, 363, 968, doi: [10.1126/science.aau8815](https://doi.org/10.1126/science.aau8815)
- Granot, J., & Sari, R. 2002, ApJ, 568, 820, doi: [10.1086/338966](https://doi.org/10.1086/338966)
- Hotokezaka, K., Nakar, E., Gottlieb, O., et al. 2018, arXiv e-prints. <https://arxiv.org/abs/1806.10596>

Table 6. Emission parameters at forward shock.

Expression	Coefficient	$u \gg 1$	$u \ll 1$
n	$4\gamma n_0$	$4n_0$	γ
e	$(\gamma - 1)n m_p c^2$	$4m_p c^2 n_0$	γ^2
B	$\sqrt{8\pi e \varepsilon_B}$	$4(2\pi)^{1/2} (m_p c^2)^{1/2} n_0^{1/2} \varepsilon_B^{1/2}$	γ
γ_m	$\frac{\bar{\varepsilon}_e e}{nm_e c^2}$	$\frac{m_p}{m_e} \bar{\varepsilon}_e$	$\frac{1}{2}\beta^2$
γ_c	$\frac{3m_e c \gamma}{4\sigma_T \varepsilon_B e t}$	$\frac{3}{16} \frac{m_e}{m_p \sigma_T c} n_0^{-1} \varepsilon_B^{-1}$	$\gamma^{-1} t^{-1}$
ε_P	$\frac{\sqrt{3}}{2} \frac{q_e^3}{m_e c^2} (p-1) n B$	$8(6\pi)^{1/2} \frac{m_p^{1/2} q_e^3}{m_e c} (p-1) n_0^{3/2} \varepsilon_B^{1/2}$	γ^2
ν_m	$\frac{3}{4\pi} \frac{q_e}{m_e c} \gamma_m^2 B$	$6(2\pi)^{-1/2} \frac{m_p^{5/2} q_e}{m_e^3} n_0^{1/2} \varepsilon_e^2 \varepsilon_B^{1/2}$	γ^3
ν_c	$\frac{3}{4\pi} \frac{q_e}{m_e c} \gamma_c^2 B$	$\frac{27}{128} (2\pi)^{-1/2} \frac{m_e q_e}{m_p^{3/2} \sigma_T^2 c^2} n_0^{-3/2} \varepsilon_B^{-3/2}$	$\gamma^{-1} t^{-2}$
E	$\frac{4\pi}{9} \rho_0 c^2 R^3 (4u^2 + 3)\beta^2$	$\frac{16\pi}{9} \rho_0 c^2$	$R^3 \gamma^2$
β_s	$\frac{4u\gamma}{4u^2 + 3}$	1	$\frac{4}{3}\beta$

Lamb, G. P., Lyman, J. D., Levan, A. J., et al. 2019, ApJL, 870, L15, doi: [10.3847/2041-8213/aaf96b](https://doi.org/10.3847/2041-8213/aaf96b)

Lazzati, D., López-Cámara, D., Cantiello, M., et al. 2017, ApJL, 848, L6, doi: [10.3847/2041-8213/aa8f3d](https://doi.org/10.3847/2041-8213/aa8f3d)

Margutti, R., Alexander, K. D., Xie, X., et al. 2018, ApJL, 856, L18, doi: [10.3847/2041-8213/aab2ad](https://doi.org/10.3847/2041-8213/aab2ad)

Mizuta, A., & Aloy, M. A. 2009, ApJ, 699, 1261, doi: [10.1088/0004-637X/699/2/1261](https://doi.org/10.1088/0004-637X/699/2/1261)

Planck Collaboration, Ade, P. A. R., Aghanim, N., et al. 2016, A&A, 594, A13, doi: [10.1051/0004-6361/201525830](https://doi.org/10.1051/0004-6361/201525830)

Ryan, G., van Eerten, H., MacFadyen, A., & Zhang, B.-B. 2015, ApJ, 799, 3, doi: [10.1088/0004-637X/799/1/3](https://doi.org/10.1088/0004-637X/799/1/3)

Troja, E., Piro, L., van Eerten, H., et al. 2017, Nature, 551, 71, doi: [10.1038/nature24290](https://doi.org/10.1038/nature24290)

Troja, E., Piro, L., Ryan, G., et al. 2018, MNRAS, 478,

118, doi: [10.1093/mnrasl/sly061](https://doi.org/10.1093/mnrasl/sly061)

van Eerten, E. T. H., Ryan, G., Ricci, R., et al. 2018, arXiv e-prints. <https://arxiv.org/abs/1808.06617>

van Eerten, H. 2018, International Journal of Modern Physics D, 27, 1842002, doi: [10.1142/S0218271818420026](https://doi.org/10.1142/S0218271818420026)

van Eerten, H., Zhang, W., & MacFadyen, A. 2010, ApJ, 722, 235, doi: [10.1088/0004-637X/722/1/235](https://doi.org/10.1088/0004-637X/722/1/235)

van Eerten, H. J., & MacFadyen, A. I. 2012, ApJL, 747, L30, doi: [10.1088/2041-8205/747/2/L30](https://doi.org/10.1088/2041-8205/747/2/L30)

Wu, Y., & MacFadyen, A. 2018, ApJ, 869, 55, doi: [10.3847/1538-4357/aae9de](https://doi.org/10.3847/1538-4357/aae9de)

Zhang, B., Fan, Y. Z., Dyks, J., et al. 2006, ApJ, 642, 354, doi: [10.1086/500723](https://doi.org/10.1086/500723)